materials

MDPI

Article

Transient Thermal Response and Simulation-Driven Machine Learning Prediction for Temperature in a Petroleum Coke Vertical Shaft Calciner

Longxin Lai [1], Jinlong Zhong [1], Jing Li [1,2,3] and Jindi Huang [1,2,3,*]

[1] School of Metallurgical Engineering, Jiangxi University of Science and Technology, Ganzhou 341000, China; 6120250206@mail.jxust.edu.cn (L.L.); z835720916jl@163.com (J.Z.); 9120200008@jxust.edu.cn (J.L.)
[2] Jiangxi Provincial Key Laboratory of High-Performance Steel and Iron Alloy Materials, Jiangxi University of Science and Technology, Ganzhou 341000, China
[3] Jiangxi Provincial Center for Interdisciplinary Studies in Future-oriented Materials, Jiangxi University of Science and Technology, Ganzhou 341000, China
* Correspondence: hjd041@163.com; Tel.: +86-15079128330

Abstract

Transient temperature evolution in a petroleum coke vertical shaft calciner (VSC) helps assess responses to operating disturbances, but transient multiphysics simulations are costly. A transient two-dimensional multiphysics model representing one pot and the flues on one side of a 24-pot, eight-layer co-current VSC, with prescribed flue temperatures, was developed to investigate step changes in flue temperature and per-pot discharge rate. Raising the upper-flue temperature by 200 K extended the high-temperature calcination zone from 1.3 to 1.9 m and shifted it upward. Increasing the discharge rate from 95 to 115 kg/h shortened this zone from 1.3 to 0.3 m and shifted it downward. The furnace wall approached a quasi-steady state within 10 h, whereas the coke bed required up to 40 h. Using 4.59×10^5 numerically generated temperature values from 510 pot-centerline locations under nine flue-temperature disturbance conditions, a Temporal Convolutional Network–Bidirectional Long Short-Term Memory–Convolutional Neural Network–Attention (TCLCA) surrogate model was developed. TCLCA achieved an R^2 of 0.997 in recursive prediction while reducing computational time by approximately 94%. The framework enables rapid prediction of simulated centerline temperature evolution.

Keywords: simulation; vertical shaft calciner; petroleum coke; machine learning; transient temperature

Check for updates

Academic Editor: Shinichi Tashiro

Received: 21 September 2026
Revised: 23 October 2026
Accepted: 24 October 2026
Published: 29 October 2026

Copyright: © 2026 by the authors. Licensee MDPI, Basel, Switzerland. This article is an open access article distributed under the terms and conditions of the Creative Commons Attribution (CC BY) license.

1. Introduction

The VSC is a key piece of equipment for calcining petroleum coke in China. The primary application of the resultant calcined coke is in the fabrication of prebaked carbon anodes used in aluminum electrolysis [1,2]. The calcination process itself involves subjecting raw petroleum coke to elevated temperatures to eliminate volatile components [3–5]. This thermal treatment enhances the material's structural density and removes undesirable impurities, thereby yielding a product that satisfies the critical specifications for electrolytic anode production.

The operating temperature inside the furnace is a decisive parameter. It significantly influences process efficiency, energy consumption, and final product quality [6,7]. Precise thermal management is, therefore, directly linked to key production metrics. Presently, conventional VSC calcination operations encounter several technical shortcomings. These

challenges encompass suboptimal strategies for recirculating calcined coke, inadequate harnessing of volatile matter released during heating, low efficiency in recovering waste heat, and abrupt disturbances in the internal temperature distribution caused by sudden operational shifts [3,8].

A fundamental challenge is the difficulty of capturing real-time, transient changes in the furnace's temperature field. This limitation frequently results in operational adjustments that are both delayed and imprecise. The consequences manifest as increased carbonaceous material loss, accelerated wear of refractory linings, and diminished quality consistency of the calcined output [9,10]. Current mitigation approaches often depend on manual intervention guided by operator expertise to tune process variables, such as fuel gas flow rate and composition, solid discharge rate, draft pressure in the flues, and feedstock particle size [11–14].

However, comprehensive monitoring of temperature variations across the entire furnace volume in real time remains impractical, constrained by both technical sensor limitations and economic considerations [15,16]. While computational fluid dynamics (CFD) simulation provides a powerful tool for accurate prediction of intricate heat and mass transfer phenomena and facilitates analysis of multi-parameter coupling effects, its application is hampered by substantial computational expenses and time requirements. Consequently, CFD alone cannot deliver the immediate feedback necessary for real-time production control.

CFD provides a useful approach for investigating the thermal behavior of vertical shaft calciners (VSCs), although transient simulations can be computationally expensive. Xiao et al. [2] developed a real-time two-dimensional mathematical model for predicting temperature distributions in petroleum coke VSCs. Zhou et al. [17] investigated the flow and temperature distributions in a petroleum coke calciner using a coupled fluid–solid CFD model and compared the calculated pressure distribution with plant measurements. Meanwhile Xiao et al. [18] analyzed petroleum coke heating using a two-fluid model. Li et al. [19] examined the effects of operating parameters on the migration of the high-temperature calcination zone, and Zheng [20] developed a three-dimensional unsteady two-fluid model to examine the effects of volatile inlet configurations, excess air coefficients, and flue outlet pressure on furnace thermal behavior, with validation against measured flue temperatures.

To improve computational efficiency, simulation-driven machine-learning methods have been applied to temperature prediction in rotary kilns [21], internal-state prediction in blast furnaces [22], and temperature uniformity optimization in wafer annealing furnaces [23]. These studies demonstrate the potential of combining numerical simulations with machine learning for efficient prediction in industrial thermal processes. A comparison of the relevant studies and their research scopes is presented in Table 1.

As summarized in Table 1, previous studies have investigated furnace thermal behavior, calcination-zone migration, and computationally efficient temperature prediction. However, further investigation is needed to characterize the time-dependent migration of the high-temperature calcination zone and the differences in thermal response times between the furnace wall and coke bed following step changes in operating parameters. In addition, the integration of multiphysics-based transient analysis with machine-learning-based recursive prediction of centerline temperature evolution in petroleum coke VSCs remains relatively limited.

To address these research needs, the present study develops a transient two-dimensional multiphysics simulation model representing a pot and its adjacent flues to investigate temperature evolution, calcination-zone migration, and thermal response times under step changes in flue temperature and per-pot discharge rate. Furthermore, TCLCA is developed

using numerically generated temperature sequences under different operating conditions to enable rapid recursive prediction of pot-centerline temperatures. Its predictive accuracy and computational efficiency are evaluated against numerical simulation results and alternative machine-learning models.

Table 1. Comparison of previous studies with the present work.

Application	Simulation Method/ML Model	Inputs/Outputs	ML Dataset Size	Difference from the Present Study
VSC [2]	Real-time 2D mathematical model	Input: Operating parameters; Output: 2D temperature field	N/A	Physics-based rapid temperature prediction
10-layer pot calciner [17]	3D fluid–solid coupled CFD model	Input: Operating boundary conditions; Outputs: Flow, pressure, and temperature fields	N/A	Flow and thermal distributions under operating conditions
24-pot calciner [18]	Two-fluid CFD model	Input: Operating conditions; Outputs: Temperature, moisture, volatile, and velocity fields	N/A	Detailed calcination-process simulation
VSC [19]	3D two-fluid model	Inputs: Discharge rate, volatile content, excess air; Outputs: Calcination-zone position and length	N/A	Parameter-dependent calcination-zone migration
56-pot, 8-layer VSC [20]	3D unsteady two-fluid CFD	Inputs: Volatile inlet configuration, excess air, outlet pressure; Outputs: Flow and temperature fields	N/A	Unsteady CFD and operating-parameter analysis
Rotary kiln [21]	CFD + GA-RF	Inputs: Operating conditions and material properties; Output: Temperature field	625 CFD cases	Temperature prediction in a different furnace type
Blast furnace [22]	Mechanistic model and ensemble ML	Inputs: Injection parameters and spatial coordinates; Outputs: Internal-state fields	270 cases; 6.43×10^6 spatial samples	Spatial internal-state prediction
Vertical annealing furnace [23]	3D FEM and RF	Inputs: Wafer spacing and heater configuration; Output: Temperature uniformity	300 simulation samples	Temperature-uniformity optimization
24-pot, 8-layer VSC (representative pot)	2D transient simulation and TCLCA	inputs: Flue temperature and discharge rate; outputs: Transient temperature field and calcination-zone migration; ML input: Historical centerline temperatures; ML output: Next-step centerline temperatures	9 disturbance cases; 4.59×10^5 temperature values	Transient step-response analysis combined with recursive temperature prediction

Note: N/A indicates that no machine-learning model was employed in the corresponding study.

2. Mathematical Model and Numerical Methods

2.1. Modelling Assumptions

The calcination of petroleum coke in VSC involves multiple coupled physical processes and chemical reactions. These processes involve petroleum coke descent, heat and mass transfer, and volatile release within the furnace.

To simplify the analysis of transient temperature field distribution, the following assumptions are made for the model:

(1) The simulation domain represents a quarter-sectional view of one pot group. The cooling water jacket region is ignored. Heat loss from the external furnace surface was neglected, whereas heat conduction through the refractory wall was included.
(2) Petroleum coke is represented as a continuous medium for the calculation of heat transfer and volatile transport within the pot.
(3) Petroleum coke descends continuously through the pot at a prescribed velocity determined by the per-pot discharge rate, as defined in Equation (3). The momentum equation is not explicitly solved.
(4) The effect of pyrolytic gas flow on the downward movement of solid petroleum coke is disregarded.
(5) The thermal conditions of the flues are represented by prescribed temperatures for individual flue layers, with a uniform temperature assumed along each corresponding boundary. The prescribed flue temperatures are independent of variations in volatile release.
(6) The progress of the pyrolysis reaction is controlled by chemical reaction kinetics. And the endothermic effects of moisture evaporation and petroleum coke pyrolysis are approximately accounted for using the effective heat capacity method, whereby the associated enthalpy changes are incorporated into the effective specific heat capacity of petroleum coke.

Under these assumptions, the numerical model focuses on transient heat transfer, species transport, and pyrolysis under prescribed coke-velocity and flue-temperature conditions.

2.2. Governing Equations

The computational domain of the VSC model is divided into two regions: the pot and the furnace body. The pot region describes the vertical descent of petroleum coke particles and the pyrolysis process of volatile matter through governing equations. The furnace body region simulates the heat transfer characteristics of the heterogeneous solid-phase zone composed of refractory bricks (silica bricks) using the energy conservation equation.

The solid-phase mass conservation equation in the pot region is given by the following:

$$\frac{\partial(\alpha\rho_s)}{\partial t} + \nabla \cdot (\alpha\rho_s \mathbf{u}) = -\sum_{i=1}^{m} R_i \tag{1}$$

$$R_i = \alpha\rho_s c_i r_i \tag{2}$$

where $\mathbf{u}$ is solid-phase velocity vector, ρ_s is the density of raw petroleum coke, R_i is the mass source term of volatile release during coke pyrolysis, α is the solid-phase filling rate, satisfying $\alpha = 1 - \varepsilon_s$, where ε_s is the void fraction of the packed petroleum coke, m is the total number of volatile components and r_i is the corresponding pyrolysis reaction rate.

The initial velocity at the inlet (v_{s0}) is expressed as follows:

$$v_{s0} = \frac{Q_m}{\alpha\rho_s A_c}, u_{s0} = 0 \tag{3}$$

where v_{s0} is the initial longitudinal (y-direction) velocity of the solid phase, Q_m is the mass flow rate of raw coke, A_c is the cross-sectional area of the pot, and u_{s0} is the

initial transverse (x-direction) velocity of the solid phase. The transient transport of volatile pseudo-components and moisture was described by Equation (4), with molecular diffusion neglected.

$$\alpha\rho\frac{\partial c_i}{\partial t} + \alpha\rho\mathbf{u}\cdot\nabla c_i = S_i \quad (4)$$

where c_i is the concentration of component i, and S_i is the corresponding reaction source term.

The heat transfer process is governed by the equation:

$$\alpha\rho C_p\frac{\partial T}{\partial t} + \alpha\rho C_p\mathbf{u}\cdot\nabla T - \nabla\cdot(K_{\text{eff}}\nabla T) = 0 \quad (5)$$

where C_p is the effective heat capacity, T is the absolute temperature, K_{eff} is the effective thermal conductivity.

The main materials in this model include petroleum coke and furnace lining materials. The key physical property parameters for petroleum coke and silica bricks are listed in Table 2, where d_p represents the equivalent particle size of petroleum coke particles.

Table 2. Physical property parameters of petroleum coke and furnace lining materials.

Material	Density, $\boldsymbol{\rho}$ ($\mathbf{kg\cdot m^{-3}}$)	Effective Heat capacity, $\mathbf{C_p}$ ($\mathbf{J\cdot kg^{-1}\cdot K^{-1}}$)	Thermal Conductivity, $\boldsymbol{\lambda}$ ($\mathbf{W\cdot m^{-1}\cdot K^{-1}}$)	Void Fraction of the Packed Petroleum Coke $\boldsymbol{\varepsilon_s}$ (-)	Reference
Petroleum coke	1700	97.35 + 26.2 × T	$(-4.084 + 2.479\times10^{-2}$ T) × $(d_p)^{0.464}$	0.58 × $(100d_p)^{0.1}$	[24,25]
Silica brick	1925	1093	$1.05 + 9.3\times10^{-4}$ T	-	[17]

The pyrolysis of petroleum coke was described using the three-stage independent parallel reaction kinetic model reported by Huang et al. [25]. The model consists of three pseudo-components, whose mass fractions and kinetic parameters are presented in Table 3. The pyrolysis reaction rate of each pseudo-component is expressed as follows:

$$r_i = Aexp\left(-\frac{E_i}{RT}\right)(1-\xi)^{n_i} \quad (6)$$

where r_i is the pyrolysis reaction rate of pseudo-component i; A is the pre-exponential factor; E_i is the activation energy; R is the universal gas constant; ξ is the pyrolysis conversion degree; and n_i is the reaction order.

Table 3. Mass fractions and reaction rates of various substances in petroleum coke pyrolysis.

Pseudo-Component	Mass Fraction	Reaction Rate, $\mathbf{s^{-1}}$	Reference
1	0.41	$1096.63\times(1-\xi)^{1.66}\times\exp(-92.36\times10^3/(8.314\times T))$	[25]
2	0.23	$1096.63\times(1-\xi)^{1.66}\times\exp(-73.52\times10^3/(8.314\times T))$	[25]
3	0.36	$1096.63\times(1-\xi)^{3.26}\times\exp(-111.15\times10^3/(8.314\times T))$	[25]

The proximate and ultimate analyses of petroleum coke were taken from Huang et al. [25]. The reported composition includes 3.00 wt.% moisture, 10.48 wt.% volatile matter, and 0.25 wt.% ash, with elemental contents of 86.98 wt.% C, 2.81 wt.% H, 1.28 wt.% O, 1.39 wt.% N, and 0.32 wt.% S. The relative mass fractions and reaction-rate expressions of the three volatile pseudo-components are presented in Table 3.

The model describes the overall release of volatile matter through three pseudo-components, with moisture release considered separately. The chemical compositions of individual gaseous products are not explicitly resolved.

2.3. Initial and Boundary Conditions

The transient simulations were initialized using the stationary solution obtained under the baseline operating conditions. Accordingly, the initial temperature and species concentration fields were prescribed as follows:

$$T(x,y,0) = T_{ss}(x,y), c_i(x,y,0) = c_{i,ss}(x,y) \quad (7)$$

where the subscript ss denotes the steady-state solution obtained under the baseline operating conditions.

The initial and boundary conditions are summarized in Table 4. Prescribed temperatures were applied to the eight flue layers (L1–L8), while the remaining thermal and species-transport boundary conditions were assigned to their corresponding boundaries.

Table 4. Initial and boundary conditions of the baseline numerical model.

Parameters	Unit	Values
Initial temperature field	K	$T_{ss}(x,y)$
Initial species concentration fields	-	$c_{i,ss}(x,y)$, i = 1, 2, 3
Petroleum coke inlet temperature	K	293
Per-pot discharge rate	$kg \cdot h^{-1}$	95
Flue temperatures (L1–L8)	K	1473.2, 1623.2, 1573.2, 1523.2, 1503.2, 1473.2, 1453.2, 1423.2
Flue inlet temperature	K	373
Initial mass fractions of volatile pseudo-components in the petroleum coke at the inlet	-	$c_{1,0} = 0.41$, $c_{2,0} = 0.23$, $c_{3,0} = 0.36$
Thermal outlet	$W \cdot m^{-2}$	$-\mathbf{n} \cdot \mathbf{q} = 0$
Symmetry and insulated boundaries	$W \cdot m^{-2}$	$-\mathbf{n} \cdot \mathbf{q} = 0$
Species no-flux boundaries	$kg/(m^2 \cdot s)$	$-\mathbf{n} \cdot \mathbf{j}_i = 0$

2.4. Numerical Solution Methods

The governing equations were solved using COMSOL Multiphysics 6.4 based on the finite element method. A stationary calculation was first performed to obtain the baseline solution, which was subsequently used to initialize the transient simulations. Both the heat-transfer and species-transport equations were included in the time-dependent calculation. The simulation time was set to 0–5000 min, with results output at 1 min intervals. The computational mesh and mesh independence study are presented in Section 3.2.

The temporal discretization employed an implicit backward differentiation formula with adaptive time stepping and variable orders of 1–2. The relative tolerance was set to 5×10^{-3}, and the absolute tolerances were controlled using a scaling factor of 0.1. The nonlinear equations were solved using a fully coupled Newton method with a damping factor of 0.9 and a maximum of eight iterations. A solution-based termination criterion was adopted, and the PARDISO direct solver was used for the linear systems.

The spatial discretization and stabilization settings were specified according to the finite-element formulations implemented in the heat-transfer and species-transport interfaces. No pressure–velocity coupling algorithm was required because the coke velocity was prescribed rather than obtained from an independently solved momentum equation.

3. Model Parameters

3.1. Geometric Structure

The three-dimensional structure of the VSC is shown in Figure 1a. Its main structure is arranged symmetrically in double rows along the XY plane. Each group of pots operates

in parallel, and adjacent pots are connected via a shared flue system to ensure uniform heat distribution.

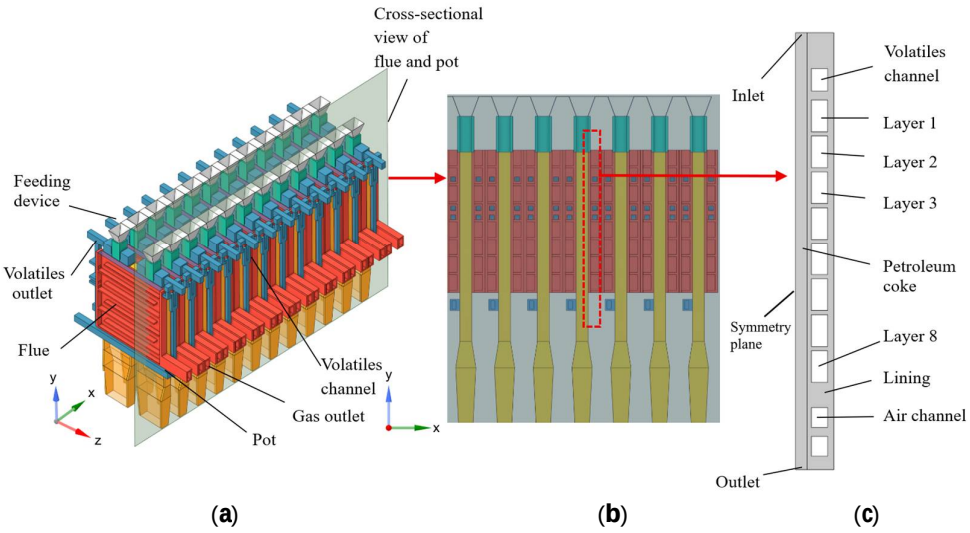


Figure 1. Structural diagram of the vertical shaft calciner (VSC): (**a**) 3D structural schematic diagram; (**b**) 2D structural schematic diagram of the VSC; (**c**) 2D simulation model of a representative pot and adjacent flues. The blue, red, yellow, and green regions represent the volatile channels, flues, pots, and feed inlets, respectively.

To investigate how changes in different operating parameters affect the transient temperature field distribution during the calcination process in the VSC, the complex furnace structure was reasonably simplified. A single pot was selected as the research object. A sectional view, extending from the inlet to the outlet and including the flues on one side, was extracted to construct the two-dimensional model shown in Figure 1c. The flue region includes a top volatile channel, a bottom air channel, and eight layers of flues, all designed as hollow structures. To simplify calculations, the flue temperatures are directly set as known values. Raw petroleum coke undergoes feeding, heating, and calcination processes, finally settling into the discharge outlet after calcination is complete.

During modeling, to highlight the core heat transfer characteristics, the influence of inspection holes and soot blowing holes on the flue gas region was neglected. The water jacket located below the pot, which has a relatively weak impact on heat transfer between the pot and the flues, was omitted to reduce computational complexity. The specific geometric parameters of the pot and flues are detailed in Table 5.

Table 5. Two-dimensional geometric parameters of the vertical shaft calciner.

Parameter Name	Value
Height of pot	6.627 m
Width of pot	0.18 m
Length of pot	1.66 m
Thickness of furnace wall	0.409 m
Thickness of flue	0.219 m
Height of flue interval	0.065 m

3.2. Mesh Generation, Independence Verification and Model Validation

Mesh size is a critical parameter affecting simulation accuracy and computational time. To verify the sufficiency of the mesh, simulations were conducted using three different mesh densities: a fine mesh (21,310 cells), a medium mesh (16,380 cells), and a coarse

mesh (8305 cells). The temperature profiles along the central axis of the pot for these three meshes are shown in Figure 2. The results from the coarse, medium, and fine meshes are virtually identical, with an average error of less than 0.1%.

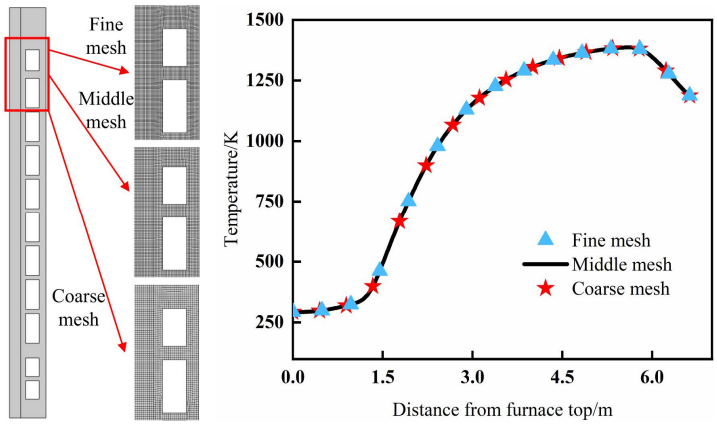


Figure 2. Mesh schematic and temperature curve distribution of mesh center.

To ensure high computational accuracy, efficiency, and to obtain a sufficient dataset of the temperature field in both the pot and flue regions, the medium mesh was selected for all subsequent simulations. The mesh consists of predominantly quad-dominant cells.

3.3. Baseline Thermal Characteristics

Figure 3 compares the simulated axial temperature distributions under baseline operating conditions with the temperature measurements reported in Refs. [7,26]. The prescribed flue-temperature profile is generally consistent with the reported measurements, supporting the selection of the thermal boundary conditions. However, noticeable discrepancies in petroleum coke temperature occur in the L3–L5 regions. These deviations may be partly attributed to the plug-flow assumption, which neglects local variations in coke descent velocity and residence time, and the two-dimensional approximation, which does not explicitly resolve three-dimensional thermal variations. In addition, uncertainties in the actual measurement locations may result in differences between the reported temperatures and the simulated pot-centerline temperatures. Notably, the predicted centerline temperature profile generally lies between the two sets of reported coke-temperature measurements over much of the L3–L5 region. This comparison provides qualitative support for the predicted axial heating trend, although the remaining discrepancies indicate limitations in the local predictive accuracy of the simplified numerical model.

Figure 4 presents the axial distributions of the residual contents of three volatile pseudo-components and the petroleum coke temperature along the pot centerline. As shown in Figures 3 and 4, the large temperature difference between the incoming petroleum coke and the adjacent L1 flue leads to rapid heating as the coke descends. The flue temperature reaches its maximum in the L2 region, providing a strong thermal driving force for coke heating and volatile release. Under the prescribed flue-temperature conditions, the increasing coke temperature promotes the progressive release of the three pseudo-components.

The release characteristics differ among the pseudo-components. Pseudo-component 2 decreases rapidly between approximately 1.2 and 1.6 m below the furnace top, corresponding to coke temperatures of approximately 400–800 K. Pseudo-component 1 is mainly released between approximately 1.4 and 1.8 m, over a temperature range of approximately 600–1000 K. In contrast, pseudo-component 3 exhibits a broader release region, with its residual content decreasing sharply between approximately 1.6 and 2.5 m as the coke temperature rises from approximately 800 to 1200 K. Most of pseudo-component 3 is released

by approximately 2.5–3.0 m, although a small residual fraction persists farther down the pot. As the coke descends through the L3–L6 regions, the decreasing temperature difference between the flues and the pot results in a slower heating rate. In the lower L7–L8 regions, the coke reaches the high-temperature calcination range, while the residual contents of the volatile pseudo-components remain close to zero.

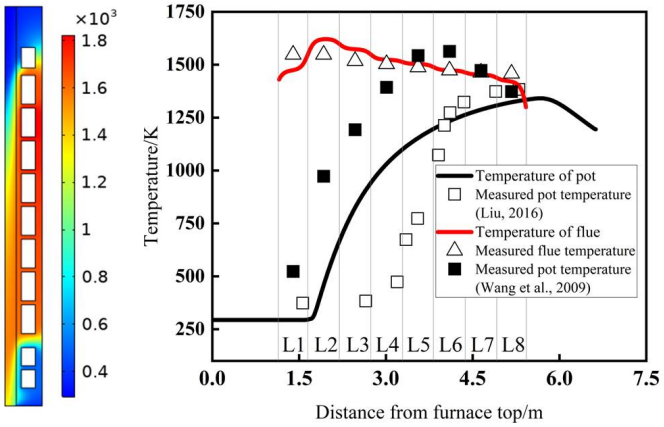


Figure 3. Temperature contour and axial simulation temperature profiles of the pot and flue versus vertical distance from furnace top. The measured pot temperature data are from Liu [26] and Wang et al. [7].

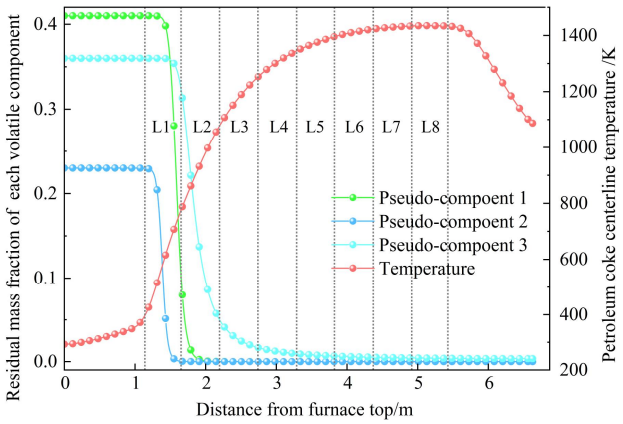


Figure 4. Axial distributions of the residual contents of the three volatile pseudo-components and petroleum coke temperature along the pot centerline.

4. Discussion of Simulation Results

4.1. Impact of Sudden Flue Temperature Change

Figure 5 shows the temperature contour and the temperature curves at the center of the pots after the flue temperature is increased by 200 K from the baseline condition. When the flue temperature increases abruptly by 200 K, the flue wall temperature rises rapidly within 5 h due to its high thermal conductivity and stabilizes after approximately 10 h. Concurrently, the high-temperature calcination zone within the pot expands, and its starting position shifts upward from L7 to the L5 region. Within the first 10 h of heating, the temperature response inside the pot is significant, and the initiation height of the high-temperature calcination zone approaches its steady-state range. After 15–20 h, the temperature field stabilizes, with temperatures in the L7 and L8 regions exceeding 1500 K, which may easily lead to coking and material blockage.

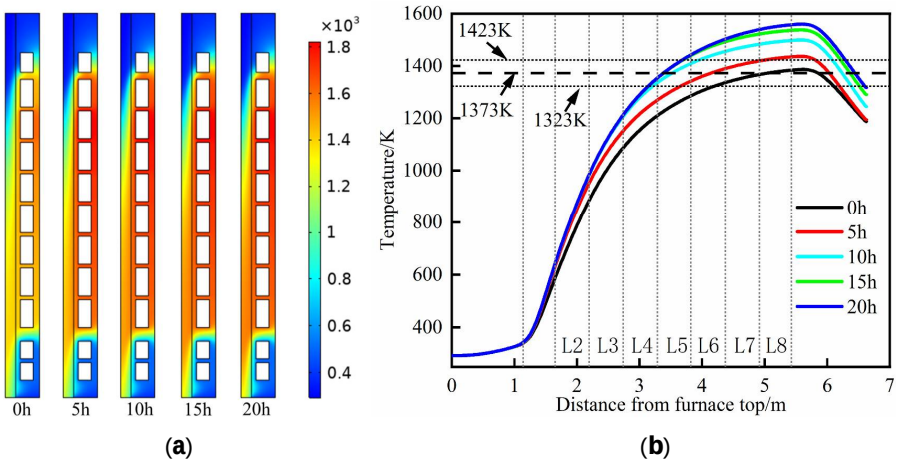


Figure 5. The temperature distribution of the model and the central temperature curve of the pot after the temperature of the flue rises by 200 K: (**a**) model temperature distribution, (**b**) central temperature curve of pot.

Figure 6 presents the temperature contour and the temperature curves at the center of the pots after the flue temperature is decreased by 200 K from the baseline condition. As shown, when the flue temperature drops abruptly by 200 K, the flue wall temperature decreases rapidly within 5 h due to high thermal conductivity, approaching a steady state after about 10 h. The high-temperature calcination zone inside the pot shifts significantly downward. By 10 h, the maximum temperature within the pot falls below 1323 K, preventing the formation of an effective high-temperature calcination zone. Between 15 and 50 h, the temperature gradually stabilizes, but the overall temperature remains below 1200 K, which may easily lead to anomalies such as the presence of uncalcined material.

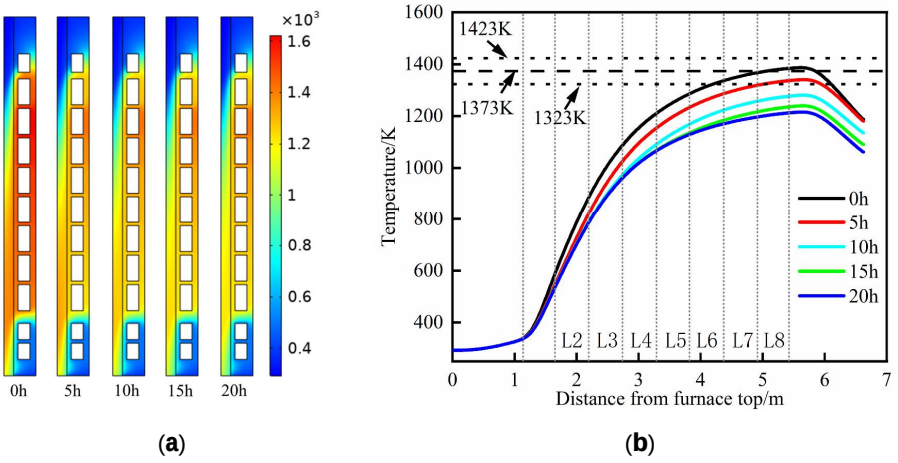


Figure 6. The temperature distribution of the model and the central temperature curve of the pot after the temperature of the flue decreases by 200 K: (**a**) model temperature distribution, (**b**) central temperature curve of pot.

In summary, the distribution of the high-temperature calcination zone along the pot center is significantly affected by changes in the overall flue temperature and responds rapidly. In actual production, the distribution of the high-temperature calcination zone can be adjusted within a short period by controlling the overall flue temperature.

4.2. Impact of Upper Flue Temperature

The L1 and L2 flues are located in the upper region of the calciner and provide the prescribed thermal boundary conditions for coke heating. Step changes in their temperatures were imposed to investigate the resulting thermal response and calcination-zone migration.

After the baseline operating condition reached a steady state, the temperatures of the L1 and L2 flues were increased or decreased by 200 K. As shown in Figure 7a, following a 200 K increase, the overall pot-centerline temperature distribution changed relatively modestly, while the coke temperatures in the L3–L5 regions increased significantly. The enhanced heat transfer from the upper flues promoted coke heating and volatile release through the temperature-dependent pyrolysis kinetics. The high-temperature calcination zone extended from 1.3 to 1.9 m, and its upper boundary shifted to the upper part of L6 after 10 h and the middle of L5 after 15 h, with the migration rate gradually decreasing. The temperature field approached a new quasi-steady state after approximately 30 h.

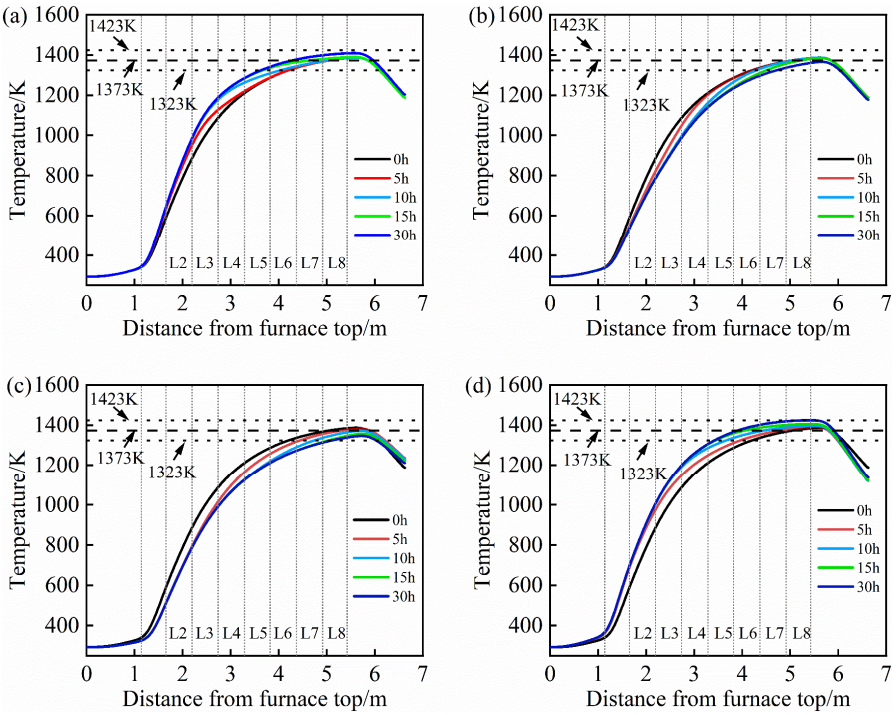


Figure 7. Time variation curve of the center temperature of the pot after sudden changes in different operating conditions: (**a**) the temperature of the upper flue suddenly increased by 200 K; (**b**) the temperature of the upper flue suddenly decreased by 200 K; (**c**) the unit discharge rate of a single pot suddenly increased from 95 kg/h to 115 kg/h; (**d**) the unit discharge rate of a single pot suddenly decreased from 95 kg/h to 75 kg/h.

As shown in Figure 7b, a 200 K decrease in the temperatures of the L1 and L2 flues primarily affected the L3–L5 regions. The reduced temperature difference between the flues and the coke bed weakened the thermal driving force for coke heating, resulting in lower coke temperatures in these regions. As the thermal disturbance propagated downward, the affected region extended to L6 after 10 h and L7 after 15 h. Meanwhile, the upper boundary of the high-temperature calcination zone gradually shifted downward, reaching the L7 region after 30 h, while its axial extent decreased from 1.3 to 0.75 m. This reduction in the high-temperature zone may increase the risk of insufficient coke calcination.

Overall, the results indicate that changes in upper-flue temperature significantly affect the axial position and extent of the high-temperature calcination zone. Appropriate

adjustment of the upper-flue temperature may therefore provide a means of regulating the thermal state of the coke bed and mitigating the risks of over- and under-calcination.

4.3. Impact of Unit Discharge Rate

The unit discharge rate per pot refers to the amount of material discharged from a single pot per unit time during the calcination of petroleum coke in the VSC. This parameter is an important means of controlling furnace conditions in production.

After the standard operating condition stabilizes, we increased or decreased the unit discharge rate by 20 kg/h. As shown in Figure 7c, an increase in the unit discharge rate shortens the coke residence time. The heat supply fails to adjust synchronously, leading to a rapid temperature drop in the middle and lower regions. After 5 h, the high-temperature calcination zone begins to shift downward, moving to the L8 region within 20 h, and its length shortens from 1.3 m to 0.3 m, easily resulting in insufficiently calcined raw material. The temperature field approached a new quasi-steady state within approximately 15 h. Under the prescribed flue-temperature conditions, the increased discharge rate shortened the residence time of petroleum coke, resulting in lower coke temperatures and a shorter high-temperature calcination zone. As shown in Figure 7d, when the unit discharge rate decreases, the material residence time increases, heat accumulates in the upper part, and the temperature in the L2–L4 regions rise significantly, while the lower part heats slowly. Within 5–30 h, the starting position of the high-temperature calcination zone shifts upward from L6 to L5, and its length increases to 2 m. As the descent of petroleum coke slows, the L7 and L8 regions experience a slight temperature rise in the later stages, and the system eventually enters a new steady state.

In summary, adjustments in the unit discharge rate significantly affect the temperature distribution and the position of the high-temperature calcination zone. Changes in the unit discharge rate influence the descent speed of petroleum coke and the time to reach steady state. However, within 5 h, the affected area of the temperature at the center of the pot is consistently the L2 to L4 region. This indicates that in the short term, the regulatory effects of natural heat diffusion and convection on temperature distribution are consistent.

5. Machine Learning Algorithm Training, Prediction, and Evaluation

Accurate prediction of the transient temperature distribution along the pot centerline is important for assessing the thermal response of vertical shaft calciners to changes in operating conditions. However, the computational cost of transient numerical simulations limits their suitability for rapid temperature prediction. Therefore, TCLCA was developed to predict the spatiotemporal evolution of centerline temperature under the evaluated flue-temperature disturbance conditions. By integrating temporal and spatial feature extraction, the model captures the thermal-response delay and spatial coupling within the calcination zone. It provides accurate predictions at substantially lower computational cost than numerical simulation, supporting rapid thermal-state evaluation and operating adjustment.

5.1. Temporal Prediction Concept

For the task of predicting the temporal evolution of temperature at the center of the pot, observation points along the centerline are used to construct temperature time series. These series characterize the temperature variation over time at each point under different operating conditions. The temporal prediction problem for the centerline temperature can be defined as follows:

$$X_k = A_{t-k}, A_{t-k+1}, \ldots, A_{t-1} \tag{8}$$

$$Y_l = (A_t, A_{t+1}, \ldots, A_{t+l-1}) \tag{9}$$

$$(A_t, A_{t+1},\ldots, A_{t+l-1}) = f(A_{t-k}, A_{t-k+1},\ldots, A_{t-1}) \quad (10)$$

where X denotes the historical temperature input sequence, A_t is the centerline temperature vector at time step t, and Y is the corresponding prediction target. The parameters k and l denote the historical input length and prediction horizon, respectively.

The TCLCA model uses historical temperature profiles at 510 locations along the pot centerline to predict the temperature profile at the next time step. Flue temperature and per-pot discharge rate are not explicitly included as model inputs. The machine-learning dataset consists of numerically generated temperature sequences under nine flue-temperature disturbance conditions. Therefore, the demonstrated predictive capability is limited to the corresponding temperature evolution, and the model has not been validated for independent changes in discharge rate.

We predicted the pot-centerline temperature by converting the one-dimensional temperature sequence into a two-dimensional matrix through the sliding window method. The historical sequence and the sequence to be predicted are respectively set as the observation window and the prediction window. The observation window contains the temperature data of k consecutive historical time steps, and the prediction window contains the temperature value of the next time step. After the prediction is completed, the two windows slide forward by one time step to generate the next set of samples until the end of the sequence. As shown in Figure 8, in this study, the historical input window contains nine consecutive temperature profiles, which are used to predict the temperature profile at the next time step. Thus, each supervised sample consists of nine input time steps and one target time step, giving a total sequence length of 10. The historical input length and total sample length are distinguished accordingly.

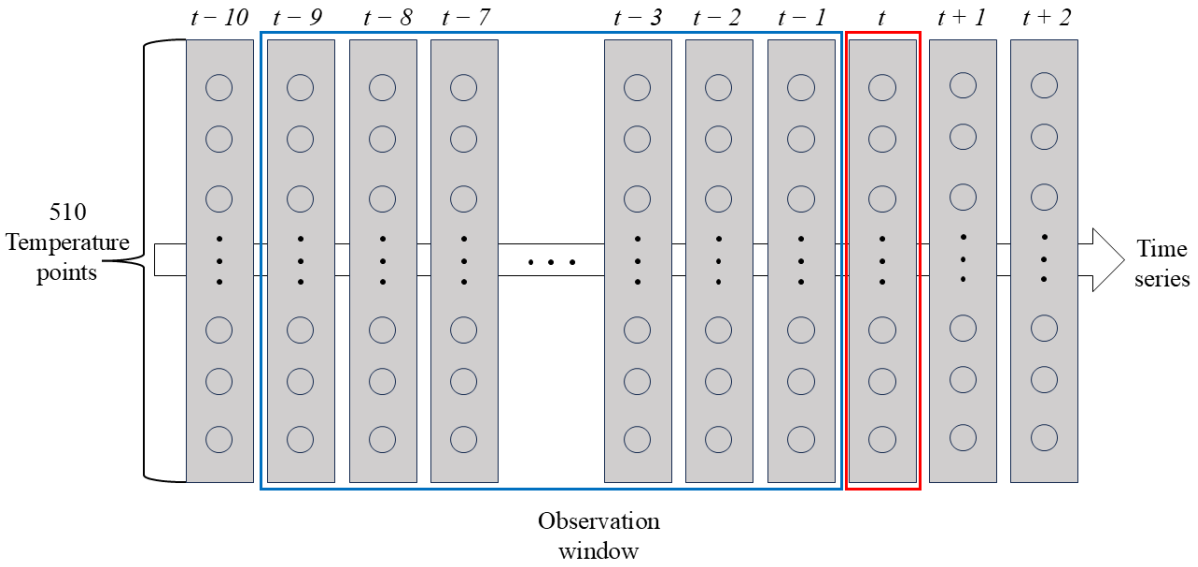


Figure 8. Time Series and Sliding Window of Temperature at the Center of the Pot (ellipsis indicates omitted time steps).

The construction of the prediction model mainly includes four different stages: data preparation, data preprocessing, model training, and prediction analysis. Figure 9 shows the workflow and methods adopted in this paper.

In the model training stage, the TCLCA model is used to train the training set, and the impact of different architectures on prediction accuracy is compared. The network is adjusted based on the prediction results obtained from the validation set to optimize its performance. The trained model is used to perform single-step and recursive predictions on

the test set, and the prediction results are compared with the simulation results to analyze the prediction ability of the model.

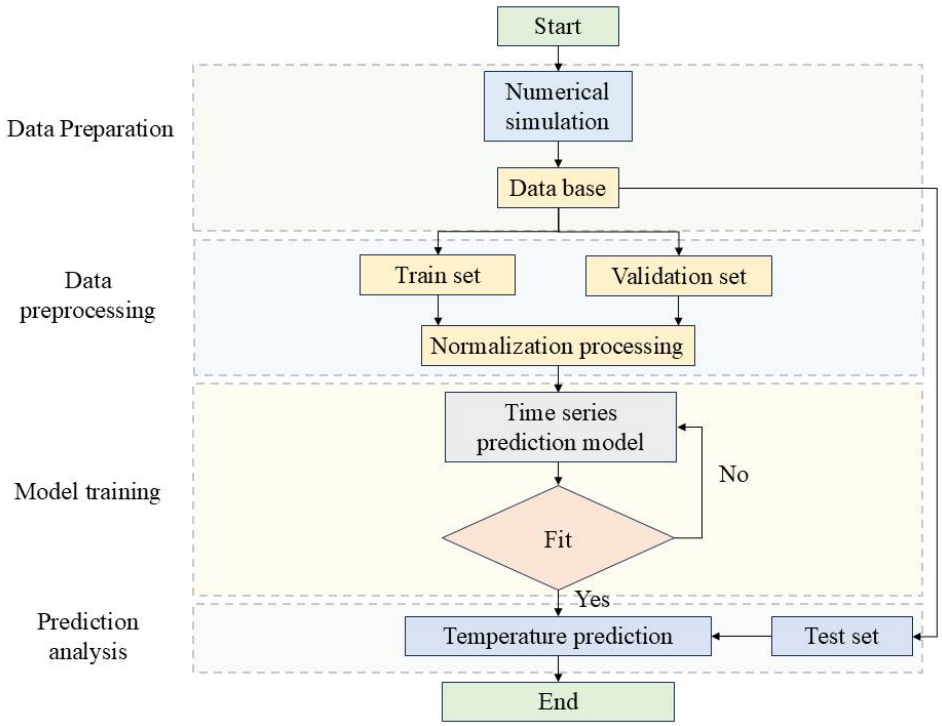


Figure 9. Workflow of simulation data-driven modeling.

5.2. Construction of the Temperature Dataset

5.2.1. Data Preparation

The annual calcination data of a certain petroleum coke smelting plant is collected and statistically analyzed. The temperature of the flues and the unit discharge rate of each pot throughout the year is analyzed. The fluctuation range of the L2 flue temperature is from 1100 K to 1580 K, the fluctuation range of the eight-layer flue temperature is from 950 K to 1300 K, and the variation range of the unit discharge rate of each pot is between 45 kg/h and 120 kg/h.

The two-dimensional pot simulation model is divided into 510 × 45 cells of approximately the same size through the square processing of quadrilateral cells. Each cell is a temperature monitoring point, and the temperature value of each point changes over time. The center temperature of the pot can be represented by a 510 × 1 one-dimensional matrix, and a time series of the center temperature of the pot is generated over time. The one-dimensional temperature matrix is composed into a two-dimensional temperature matrix through the observation window as the input to predict the center temperature of the pot at the next moment. The specific operation is shown in Figure 8.

Based on the transient thermal-response analysis, nine flue-temperature disturbance conditions were simulated to generate the temperature dataset. Taking the L2 flue as an example, its temperature was changed from the baseline value of approximately 1623 K to 1423, 1473, 1523, 1573, 1673, 1723, 1773, 1823, and 1873 K. Seven conditions were used for training, while the 1823 K and 1873 K conditions were reserved for validation and independent testing, respectively. The datasets were divided by operating condition rather than by individual time windows. For each condition, 100 centerline temperature profiles, each containing 510 spatial points, were sampled at 0.2 h intervals from 0 to 19.8 h, yielding a total of 4.59×10^5 temperature values.

5.2.2. Data Preprocessing

The numerically generated centerline temperature data were preprocessed before model training. The nine operating conditions were first divided into training, validation, and test sets. Min–Max scaling parameters were determined independently for each of the 510 centerline locations using only the training input sequences. The same parameters were subsequently applied to the training targets and the validation and test datasets without refitting, thereby preventing information leakage from the held-out conditions. The fitted scaling parameters were also used to transform the predicted temperatures back into physical units for performance evaluation. The Min–Max transformation is expressed as follows:

$$x' = \frac{x - Min}{Max - Min} \tag{11}$$

where x and x′ denote the original and normalized temperature values, respectively; *Min* and *Max* represent the minimum and maximum temperature values at the corresponding centerline location, determined exclusively from the training input sequences.

5.2.3. Model Evaluation Indicators

To evaluate the prediction performance, we adopted the following three typical evaluation indicators.

$$MSE = \frac{1}{n}\sum_{i=1}^{n}(y_i - y_i^*)^2 \tag{12}$$

$$MAE = \frac{1}{n}\sum_{i=1}^{n}|y_i - y_i^*| \tag{13}$$

$$R^2 = 1 - \frac{\sum_{i=1}^{n}(y_i - y_i^*)^2}{\sum_{i=1}^{n}(y_i - \overline{y}_i)^2} \tag{14}$$

where n represents the number of samples, y_i is the true value of the i-th sample, y_i^* is the predicted value of the i-th sample, and $\overline{y}_i$ is the average of the true values.

5.3. Model Architecture

The dual-channel spatiotemporal feature fusion pot-centerline temperature prediction model TCLCA introduced in this paper is mainly divided into four modules, including the TCN-BiLSTM layer, the CNN-Attention layer, the feature fusion layer, and the temperature prediction output layer. The overall model is shown in Figure 10:

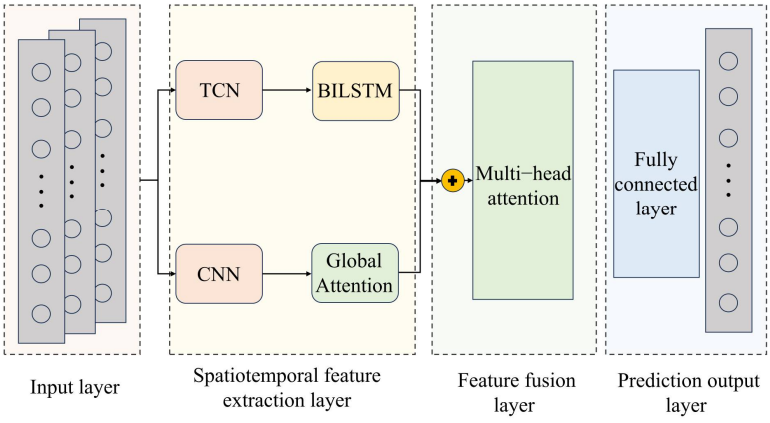


Figure 10. Architecture of the dual-channel spatiotemporal feature fusion temperature prediction model.

5.3.1. TCN-BiLSTM

The TCN-BiLSTM layer combines the Temporal Convolutional Network (TCN) and BiLSTM to fully leverage the advantages of both, making the model more robust. The structure of TCN is shown in Figure 11.

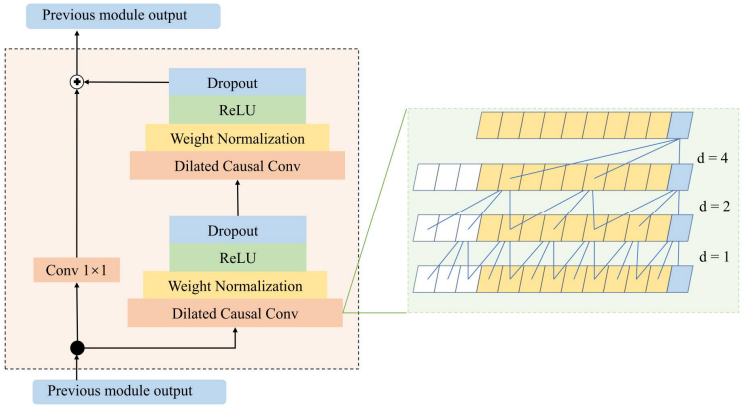


Figure 11. Schematic diagram of the TCN structure.

TCN introduces dilated convolution, which inserts intervals between the elements of the convolution kernel, causing the receptive field of each layer of convolution to expand exponentially, thereby effectively capturing the long-term dependencies of the input data. For a given input sequence and convolution kernel, the output y_t at time t of dilated convolution satisfies:

$$y_t = \sum_{i=0}^{k-1} f_i x_{t-d \cdot i} \tag{15}$$

where k is the size of the convolution kernel, and d is the dilation rate, which determines the actual spacing between the elements of the convolution kernel.

For a given input X_{TCN} and convolution operation $F(x)$, the output of the residual connection can be expressed as:

$$H(X_{TCN}) = F(X_{TCN}) + X_{TCN} \tag{16}$$

where F(x) is the output of the convolutional layer or multiple convolution operations and nonlinear activation functions, and x is the original input.

To enhance the model's ability to extract bidirectional hidden features at different time scales, the output h of the TCN is used as the input to the BiLSTM. The formula is as follows:

$$\vec{h_t} = LSTM(\vec{x_t}, \vec{h_{t-1}}) \tag{17}$$

$$\overleftarrow{h_t} = LSTM(\vec{x_t}, \overleftarrow{h_{t+1}}) \tag{18}$$

$$H_t = [\vec{h_t} \oplus \overleftarrow{h_t}] \tag{19}$$

where $\vec{h_t}$ and $\overleftarrow{h_t}$ are the outputs of the forward and backward LSTM at time t, respectively, $\vec{h_t}$ is the input at time t, and $\oplus$ denotes the vector concatenation operation.

By combining TCN and BiLSTM, the model integrates multi-scale temporal feature extraction with bidirectional sequence modeling to capture complex temperature evolution patterns.

5.3.2. CNN-Attention

The CNN-Attention layer primarily consists of two core components: a multi-channel residual CNN module and a global attention module. In the prediction of the pot temperature, the temperature at different points is jointly influenced by local heat conduction and

the global ambient temperature. The multi-channel design enables the model to simultaneously focus on local temperature fluctuations and spatial correlations over a larger range, thereby enhancing the comprehensiveness of feature representation.

Residual connections directly add the input to the convolutional output. Meanwhile, 1 × 1 convolutions align channel dimensions. This ensures consistent feature map shapes throughout the network.

The formula for the residual connection is as follows:

$$Y = F(X_{CNN}) + X_{CNN} \tag{20}$$

where Y is the input to the next layer, $F(X)$ is the output after the convolution operation, and X_{CNN} is the input to the current layer. If the dimensions of the input and output do not match, a 1 × 1 convolution is applied to X_{CNN} for a linear transformation to align the dimensions. The application of residual connections effectively mitigates the vanishing gradient problem in the network, ensuring stable gradient propagation.

The Global Attention Mechanism aims to capture global spatial dependencies by weighting the features at all positions. In the heat conduction process of the petroleum coke pot, the evolution of the temperature field, induced by the settling of petroleum coke, exhibits significant spatial and temporal hysteresis. For a specific temperature measurement point on the centerline of the pot, its current temperature is influenced by the temperatures at points above it at previous times. The global attention mechanism dynamically adjusts the weights of different positions, highlighting the spatial features most critical for predicting the target, thereby enhancing the model's ability to understand the global temperature distribution.

The output of the multi-channel residual CNN module is weighted by the global attention mechanism to form the final spatial feature representation of the temperature evolution over time at the center of the VSC pot. This process achieves effective fusion of local and global features.

5.3.3. Feature Fusion

The feature fusion layer integrates temporal and spatial features extracted by the TCN-BiLSTM and CNN-Attention layers. This integration enables the model to capture both local and global information in temperature time-series data effectively.

The Multi-Head Attention mechanism is a core component of the Transformer model. It is based on the self-attention principle. The mechanism involves three main steps. First, input features are linearly transformed into three vectors: Query (Q), Key (K), and Value (V). Second, scaled dot-product attention calculates the attention weights for each head. Finally, outputs from all heads are concatenated and linearly transformed into the final representation.

For the i-th attention head, the attention score is computed as follows:

$$Attention(Q_i, K_i, V_i) = \text{softmax}\left(\frac{Q_i K_i^T}{\sqrt{d_k}}\right) V_i \tag{21}$$

where $\sqrt{d_k}$ is a scaling factor. It reduces numerical instability in high-dimensional dot products.

Each attention head independently focuses on different feature subspaces. This allows multi-perspective analysis of the input. The feature fusion calculation is defined as:

$$Head_i = Attention(QW_i^Q, KW_i^K, VW_i^V) \tag{22}$$

$$x = Concat(head_1, \ldots, head_k)W \tag{23}$$

Multi-head attention offers advantages in parallel computation and multi-view feature extraction. It dynamically assigns weights to adaptively fuse local temporal patterns with global spatial thermal relationships. This enhances the integration of spatiotemporal features and improves the model's sensitivity to critical information.

5.3.4. Temperature Prediction

The fused features are flattened and fed into the prediction output layer. Dropout regularization is applied to enhance generalization and prevent overfitting. A fully connected layer then performs linear mapping on the fused features. This produces the predicted temperature profile at all 510 locations along the pot centerline.

5.4. Experimental Training

5.4.1. Experimental Setup

The model was trained under the following environment: GPU: GTX 1050; OS: Windows 11 64-bit; Programming Language: Python 3.8; Framework: TensorFlow 2.8.2; CUDA Version: 11.1. Specific model hyperparameters are listed in Table 6.

Table 6. Hyperparameter Settings.

Parameter	Value
epochs	200
patience	20
batch	16
lr	0.0001
Historical input length	9
Prediction horizon	1
Total sequence length	10

The Adam optimizer was used throughout the experiments. The cosine annealing scheduler was applied to adjust the learning rate periodically via a cosine function [27]. This approach improves the model's training effectiveness.

The TCLCA model was tested under working conditions using single-step and recursive prediction. This procedure validated its prediction performance relative to simulation models. The results are shown in Figures 12 and 13.

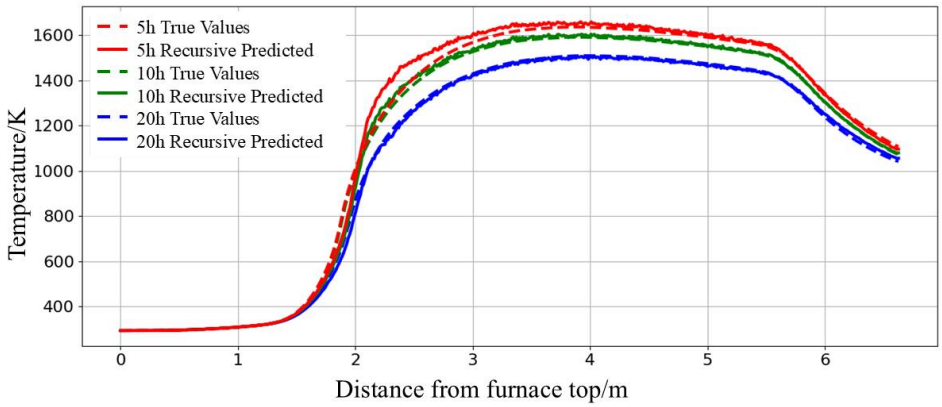


Figure 12. Comparison of single-step prediction results.

In single-step prediction, the model uses the preceding nine centerline temperature profiles to predict the temperature profile at the next time step. Recursive prediction was initialized using the first nine Numerically generated centerline temperature profiles of the

test condition. The model then generated 91 consecutive temperature profiles by feeding each predicted profile back into the input window, without using additional simulation temperature values during the recursive process. These predictions were compared with the corresponding numerically generated profiles within the available simulation interval. Therefore, the reported results assess recursive prediction accuracy and error accumulation within the simulated time range, rather than temporal extrapolation beyond that range.

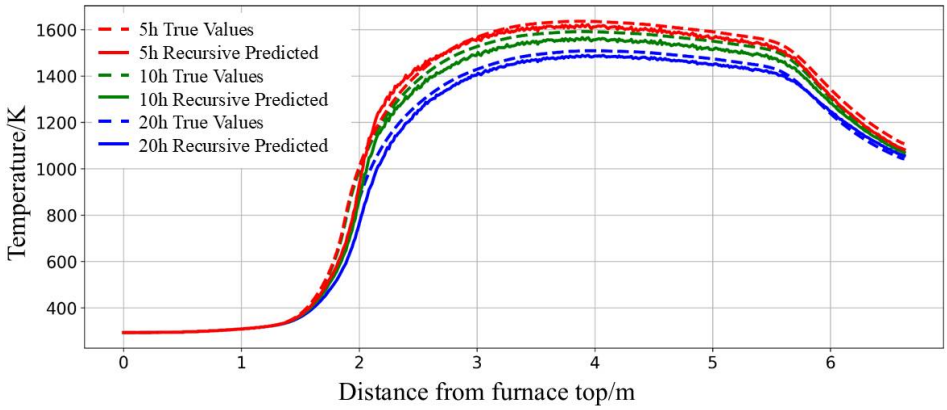


Figure 13. Comparison of recursive prediction results.

The single-step predictions closely match the actual simulated values. This indicates excellent short-term prediction capability. The recursive prediction results align well with the true curve in high-temperature calcination and low-temperature zones. A slight deviation appears near the furnace top toward the end of the prediction period. Overall, the prediction error remained limited over the evaluated recursive sequence, indicating satisfactory predictive accuracy under the held-out test condition.

For the evaluated centerline temperature sequence covering a physical simulation period of 0–1200 min, the numerical simulation required 161 s of computational time, whereas TCLCA recursive inference required approximately 10 s for the corresponding prediction task. This represents a reduction in computational time of approximately 94%.

5.4.2. Comparative Experiments

Comparative experiments evaluated the TCLCA model against other time series forecasting models. Performance was measured using MAE, MSE, and R^2 metrics. Results are provided in Tables 7 and 8.

The following models were compared:

(1) FC-LSTM [28]: This model uses an LSTM network to capture temporal dependencies. A fully connected layer produces the final prediction.
(2) Transformer: The Transformer employs multi-head attention and is widely used in time series tasks.
(3) LSTNet [29]: This model combines CNN and LSTM to extract short-term local dependencies and long-term trends. An autoregressive component addresses scale insensitivity.
(4) DGCnetwork [30]: A three-layer GRU extracts temporal features. A CNN captures spatial features. A fully connected layer integrates these features for prediction.

Under the evaluated test condition, TCLCA outperformed the comparison models in both single-step and recursive prediction, demonstrating its effectiveness for the investigated temperature-prediction task.

Table 7. Performance comparison of TCLCA model with other time series prediction models in single-step prediction.

Model	MSE (Normalized)	MAE (Normalized)	R^2
FC-LSTM	0.0187	0.0862	0.9974
Transformer	0.0104	0.0617	0.9981
LSTNet	0.0148	0.0672	0.9980
DGCnetwork	0.0162	0.0864	0.9971
TCLCA	0.0088	0.0538	0.9986

Table 8. Performance comparison of TCLCA model with other time series prediction models in recursive prediction.

Model	MSE (K^2)	MAE (K)	R^2
FC-LSTM	10,056.3923	76.8593	0.9608
Transformer	1012.8434	21.4567	0.9837
LSTNet	7384.5594	68.1689	0.9723
DGCnetwork	7084.2267	65.5653	0.9724
TCLCA	760.6533	18.6888	0.9970

5.4.3. Ablation Experiments

Ablation experiments were conducted to evaluate the impact of each component in the TCLCA model on temperature prediction performance. The results are shown in Tables 9 and 10. Evaluation metrics include MSE, MAE, and R^2.

Table 9. Results of ablation experiments for TCLCA model.

Model	MSE (Normalized)	MAE (Normalized)	R^2
TCLCA-TCN	0.0128	0.0708	0.9978
TCLCA-BiLSTM	0.0130	0.0679	0.9983
TCLCA-CNN	0.0189	0.0892	0.9969
TCLCA-Attention	0.0145	0.0713	0.9981
TCLCA	0.0088	0.0538	0.9986

Table 10. Recursive prediction results of different variants in TCLCA model ablation experiments.

Model	MSE (K^2)	MAE (K)	R^2
TCLCA-TCN	7398.4624	65.0351	0.9712
TCLCA-BiLSTM	16,825.9506	95.6531	0.9345
TCLCA-CNN	8793.4323	68.5235	0.9658
TCLCA-Attention	48,996.5712	162.3139	0.8093
TCLCA	760.6533	18.6888	0.9970

Four variant models were designed:

(1) TCLCA-TCN variant: The TCN module was removed from the temporal feature channel. Only BiLSTM was used for temporal feature extraction.
(2) TCLCA-BiLSTM variant: The BiLSTM module was removed from the temporal feature channel. Only the multi-scale dilated TCN was used for feature extraction.
(3) TCLCA-CNN variant: The CNN-Attention layer was removed from the spatial feature extraction branch. The model relied solely on the TCN-BiLSTM layer.
(4) TCLCA-Attention variant: The multi-head attention mechanism was removed from the feature fusion process. Simple concatenation was used instead.

Experimental results show that the complete TCLCA model outperforms all ablation variants across all metrics. Removing the TCN module weakened the model's ability to capture temporal features. Removing BiLSTM limited the model's capacity for modeling bidirectional temporal relationships. Removing the CNN module significantly reduced the model's ability to model spatial information. Removing the multi-head attention mechanism led to decreased performance and larger prediction deviations. This confirms the advantage of the attention mechanism in integrating spatiotemporal features.

The TCLCA model maintains low error accumulation and high fitting accuracy in long-term recursive prediction. All ablation variants show performance degradation. Removing the TCN module weakens long-term temporal feature capture, causing a slight error increase. Removing the BiLSTM causes significant performance deterioration. This confirms its important role in modeling temporal dependencies and long-term trends. Compared with single-step prediction, the CNN-Attention layer shows smaller error accumulation in recursive prediction. The absence of spatial features has less impact in long-term recursive scenarios. Removing the multi-head attention mechanism causes a sharp error increase and significant R^2 drop. This suggests an important contribution in feature fusion for long-term recursive prediction.

As TCLCA was trained exclusively on numerically generated temperature data, its predictive accuracy is inherently dependent on the reliability of the underlying numerical model. The discrepancies observed in the L3–L5 regions (Figure 3) may therefore propagate to the surrogate predictions. Accordingly, the reported prediction accuracy reflects agreement with numerical results rather than direct validation against actual furnace temperatures.

The TCLCA model achieved satisfactory predictive accuracy under the held-out test condition. Further evaluation under additional operating conditions would provide a more comprehensive assessment of its generalizability.

6. Conclusions

A transient two-dimensional multiphysics simulation model was developed to investigate the thermal response of a petroleum coke vertical shaft calciner under changes in flue temperature and per-pot discharge rate. The results showed that increasing the flue temperature shifted the high-temperature calcination zone upward and increased its axial extent, whereas increasing the discharge rate shortened the residence time of petroleum coke and displaced the high-temperature zone downward, thereby increasing the risk of insufficient calcination. Following a step change in operating conditions, the furnace wall approached a quasi-steady thermal state within approximately 10 h, while the coke bed exhibited a slower thermal response and required up to approximately 40 h to reach a quasi-steady temperature distribution.

Based on the numerical simulations, 4.59×10^5 spatiotemporal temperature values from 510 centerline locations under nine flue-temperature disturbance conditions were constructed as a dataset for surrogate modeling. A hybrid machine learning surrogate, TCLCA, was developed to predict the transient evolution of centerline temperature. In recursive prediction, the surrogate achieved an R^2 of 0.997 and an MAE of 18.69 K over the evaluated transient sequence. For the same centerline temperature sequence, the calculation time was reduced from 161 s using the numerical model to approximately 10 s using surrogate-model inference, corresponding to a reduction of about 94% under the reported computational conditions.

Overall, the proposed simulation-driven surrogate framework provides an efficient approach for rapidly predicting transient temperature evolution and assessing calcination-zone migration in petroleum coke vertical shaft calciners. The numerical model provides insight into the thermal responses to flue-temperature and discharge-rate disturbances,

while TCLCA enables rapid prediction of centerline temperature evolution under the evaluated flue-temperature disturbance conditions.

Author Contributions: L.L.: Methodology, Writing—review and editing; J.Z.: Conceptualization, Validation, Formal analysis, Writing—review and editing; J.H.: Investigation, Funding acquisition, Supervision, Validation, Formal analysis, Writing—original draft; J.L.: Investigation, Funding acquisition, Supervision, Conceptualization, Writing—review and editing. All authors have read and agreed to the published version of the manuscript.

Funding: This work is financially supported by the Jiangxi Provincial Natural Science Foundation of China (20242BAB25251), the National Natural Science Foundation of China (52004112), the Program of Qingjiang Excellent Young Talents of Jiangxi University of Science and Technology (JXUSTQJYX2020016), the Scientific Research Foundation of Jiangxi University of Science and Technology (205200100517), the Jiangxi Provincial Key Laboratory of High-Performance Steel and Iron Alloy Materials (2024SSY05041) and the Pioneer Research Program of Jiangxi Provincial Center for Interdisciplinary Studies in Future-oriented Materials (204204200158).

Data Availability Statement: The numerically generated temperature data and machine-learning prediction results supporting the findings of this study are available from the corresponding author upon reasonable request.

Conflicts of Interest: The authors declare that they have no conflicts of interest.

Abbreviations

Nomenclature	
Symbols	
VSC	Vertical shaft calciner
TCLCA	Temporal Convolutional Network–Bidirectional Long Short-Term Memory–Convolutional Neural Network–Attention
CFD	Computational Fluid Dynamics
TCN	Temporal Convolutional Network
BiLSTM	Bidirectional Long Short-Term Memory
CNN	Convolutional Neural Network
LSTM	Long Short-Term Memory
GRU	Gated Recurrent Unit
FC-LSTM	Fully Connected LSTM
LSTNet	Long- and Short-Term Time-series Network
DGCnetwork	Deep GRU-CNN Network
RFR	Random Forest Regression
GA-RF	Genetic Algorithm-Optimized Random Forest
MSE	Mean Squared Error
MAE	Mean Absolute Error
R^2	Coefficient of Determination
Variables	
u	Solid-phase velocity vector (m/s)
ρ	Density (kg·m^{-3})
ρ_s	Density of raw petroleum coke (kg·m^{-3})
m	Total number of volatile components (–)
α	Solid-phase filling rate (–)
ξ	pyrolysis conversion degree (–)
v_{s0}	Initial longitudinal solid-phase velocity (m/s)
u_{s0}	Initial transverse solid-phase velocity (m/s)
Q_m	Mass flow rate of raw coke (kg/s)
A_c	Cross-sectional area of the pot (m^2)
C_p	Effective specific heat capacity (J·kg^{-1}·K^{-1})
K_{eff}	Effective thermal conductivity (W·m^{-1}·K^{-1})
S_i	corresponding reaction source term (kg·m^{-3}·s^{-1})
d_p	Equivalent particle size of petroleum coke (m)
Y	Input of the residual connection (–)
T	Temperature (K)
t	Time (s or h)
n	Number of samples (–)
y_i	True value of the i-th sample (–)
y_i^*	Predicted value of the i-th sample (–)
x	Original data (K)
x'	Result after normalizing x (–)
Min	Minimum training temperature at the corresponding location (K)
Max	Maximum training temperature at the corresponding location (K)
k	Size of the convolution kernel (–)
X_{TCN}	TCN input (–)
X_{CNN}	CNN input (–)
$\sqrt{d_k}$	Scaling factor to stabilize the dot-product calculation (–)
Q, K, V	Query, Key, and Value matrices (–)
QW_i^Q, KW_i^K, VW_i^V	Linear projection weight matrices for the i-th attention head (–)
$head_i$	Output feature map of the i-th attention head (–)

ε_s	Void fraction of packed petroleum coke (–)	W	Final linear projection weight matrix for feature concatenation (–)
R_i	Mass source term of volatile release during pyrolysis ($kg \cdot m^{-3} \cdot s^{-1}$)		

References

1. Chen, S.Y.; Zhang, Q.; Mclellan, B.; Zhang, T.T. Review on the petroleum market in China: History, challenges and prospects. *Pet. Sci.* **2020**, *17*, 1779–1794. [CrossRef]
2. Xiao, J.; Huang, J.; Zhong, Q.; Li, F.; Zhang, H.; Li, J. A real-time mathematical model for the two-dimensional temperature field of petroleum coke calcination in vertical shaft calciner. *JOM* **2016**, *68*, 2149–2159. [CrossRef]
3. Sun, Y.; Xu, H.; Wang, Y.; Cui, Y.; Liu, C. The comparison between vertical shaft furnace and rotary kiln for petroleum coke calcination. In *Light Metals 2010*; Johnson, J.A., Ed.; The Minerals, Metals & Materials Society: Warrendale, PA, USA, 2010; pp. 917–921.
4. Lin, P.; Ji, J.; Luo, Y.; Wang, Y. A non-isothermal integrated model of coal-fired traveling grate boilers. *Appl. Therm. Eng.* **2009**, *29*, 3224–3234. [CrossRef]
5. Amara, B.; Kocaefe, D.; Kocaefe, Y. A review of the studies on the utilization of petroleum pitch and its blends with coal tar pitch for carbon anode production in aluminum industry. *Next Res.* **2025**, *2*, 100250. [CrossRef]
6. Lan, Y.; Wang, S.; Zhang, W.; Mu, L.; Lu, J. Effect of operation parameters on waste heat recovery on the coke surface of periodic graphitization furnaces. *Case Stud. Therm. Eng.* **2022**, *36*, 102149. [CrossRef]
7. Wang, P.; Luo, Y.; Gong, Z.; Li, Q.; Tan, Z.; Jia, L.; Yu, Y. Analysis on petroleum coke calcination technologies for vertical shaft furnaces in China. *Carbon Tech.* **2009**, *28*, 41–45. (In Chinese)
8. Huang, J.; Lu, H.; Li, J.; Yang, Y. Resistance characteristics and particle movement behavior of a petroleum coke particle packed bed in a vertical shaft calciner under different burden distribution methods. *Asia-Pac. J. Chem. Eng.* **2024**, *19*, e3105. [CrossRef]
9. Yin, C.J. Temperature and pressure detection and control system of an anode vertical shaft furnace. *Light Met.* **2018**, 59–62. (In Chinese) [CrossRef]
10. Hou, J.; Jiang, X.Y. Application of an automatic temperature control system in a vertical shaft furnace. *Light Met.* **2025**, 31–34. (In Chinese) [CrossRef]
11. Li, J.; Huang, J.; Zhou, S. Reconstruction of pore structures in petroleum coke packed beds utilizing CT scanning and CFD simulation of resistance characteristics. *Processes* **2025**, *13*, 3272. [CrossRef]
12. Li, X.K.; Zhou, S.H.; Liu, C.D.; Liu, C.; Sun, Y. Simulation research and application of premixed stable combustion technology for petroleum coke calcination in a vertical shaft furnace. *Light Met.* **2025**, 13–18. (In Chinese) [CrossRef]
13. Li, Z.T.; Li, C.M.; Wang, D.D.; Zi, M.G.; Duan, B.; Wu, J.M.; Li, C.W. Discussion and improvement on several main problems of vertical shaft furnaces. *Yunnan Metall.* **2022**, *51*, 160–164. (In Chinese)
14. Zhang, Z.G.; Zhou, J.; Zhao, F.L. Cause analysis and countermeasures for early damage of the charge tank in a vertical shaft furnace. *Light Met.* **2025**, 22–27. (In Chinese) [CrossRef]
15. Leng, X.Z.; Li, Y.B.; Lu, B. Monitoring scheme for furnace temperature and pressure of a vertical shaft furnace based on Modbus RTU fieldbus. *Light Met.* **2018**, 55–57, 64. (In Chinese) [CrossRef]
16. Yang, Q. Temperature and pressure measurement system of a vertical shaft furnace based on CAN-bus 2.0. *Light Met.* **2021**, 58–62. (In Chinese) [CrossRef]
17. Zhou, S.H.; Sun, Y.; Liu, C.D. Numerical simulation study of a vertical shaft furnace. *Light Met.* **2013**, 33–36, 42. (In Chinese) [CrossRef]
18. Xiao, J.; Huang, J.; Zhong, Q.; Zhang, H.; Li, J. Modeling and simulation of petroleum coke calcination in pot calciner using two-fluid model. *JOM* **2016**, *68*, 643–655. [CrossRef]
19. Li, J.; Huang, J.; Xiao, J.; Li, M. Simulation of migration of high temperature zone of petroleum coke layer in a vertical shaft furnace. *Chin. J. Nonferrous Met.* **2018**, *28*, 1216–1224. (In Chinese) [CrossRef]
20. Zheng, X. Numerical Simulation of the Thermal Process of a Vertical Shaft Furnace. Master's Thesis, University of Science and Technology Liaoning, Anshan, China, 2022. [CrossRef]
21. Wang, Y.; Xu, Y.; Song, X.; Sun, Q.; Zhang, J.; Liu, Z. Novel method for temperature prediction in rotary kiln process through machine learning and CFD. *Powder Technol.* **2024**, *439*, 119649. [CrossRef]
22. Wu, W.; Kuang, S.; Jiao, L.; Yu, A. A machine learning model for quickly predicting the inner states of ironmaking blast furnaces. *Powder Technol.* **2024**, *445*, 120137. [CrossRef]
23. Yang, S.K.; Dezfoli, A.R.A. Machine-learning-assisted finite-element optimization of temperature uniformity in a vertical annealing furnace for silicon wafers. *Mater. Lett.* **2026**, *406*, 139919. [CrossRef]

24. Huang, J.; Lu, H.; Li, J.; Yang, Y. Heat transfer characteristics of petroleum coke particle packed bed: An experimental and CFD simulation study. *Asia-Pac. J. Chem. Eng.* **2025**, *20*, e3174. [CrossRef]
25. Huang, J.; Zhang, D.; Li, J. Influence mechanism of migration path of petroleum coke pyrolysis volatiles in a vertical shaft furnace. *J. Cent. South Univ.* **2023**, *54*, 465–476. (In Chinese)
26. Liu, Q. Discussion on temperature distribution of cocurrent vertical shaft furnace and related problems. *Carbon Tech.* **2016**, *35*, 64–65. (In Chinese)
27. Tubishat, M.; Ja'afar, S.; Idris, N.; Al-Betar, M.A.; Alswaitti, M.; Jarrah, H.; Ismail, M.A.; Omar, M.S. Improved sine cosine algorithm with simulated annealing and singer chaotic map for Hadith classification. *Neural Comput. Appl.* **2022**, *34*, 1385–1406. [CrossRef]
28. Zhang, Q.; Wang, H.; Dong, J.; Zhong, G.; Sun, X. Prediction of sea surface temperature using long short-term memory. *IEEE Geosci. Remote Sens. Lett.* **2017**, *14*, 1745–1749. [CrossRef]
29. Lai, G.; Chang, W.C.; Yang, Y.; Liu, H. Modeling long- and short-term temporal patterns with deep neural networks. In Proceedings of the 41st International ACM SIGIR Conference on Research & Development in Information Retrieval, Ann Arbor, MI, USA, 8–12 July 2018; pp. 95–104. [CrossRef]
30. Yu, X.; Shi, S.; Xu, L.; Liu, Y.; Miao, Q.; Sun, M. A novel method for sea surface temperature prediction based on deep learning. *Math. Probl. Eng.* **2020**, *2020*, 6387173. [CrossRef]

Disclaimer/Publisher's Note: The statements, opinions and data contained in all publications are solely those of the individual author(s) and contributor(s) and not of MDPI and/or the editor(s). MDPI and/or the editor(s) disclaim responsibility for any injury to people or property resulting from any ideas, methods, instructions or products referred to in the content.